

# Radial Tully-Fisher relation and the local variance of Hubble parameter

Balakrishna S. Haridasu,<sup>1,2,3\*</sup> Paolo Salucci,<sup>1,2†</sup> Gauri Sharma,<sup>1,2,3,4,5,6</sup>

<sup>1</sup>*SISSA-International School for Advanced Studies, Via Bonomea 265, 34136 Trieste, Italy*

<sup>2</sup>*INFN, Sezione di Trieste, Via Valerio 2, I-34127 Trieste, Italy*

<sup>3</sup>*IFPU, Institute for Fundamental Physics of the Universe, via Beirut 2, 34151 Trieste, Italy*

<sup>4</sup>*Department of Physics and Astronomy, University of the Western Cape, Cape Town 7535, South Africa*

<sup>5</sup>*University of Strasbourg, CNRS UMR 7550, Observatoire astronomique de Strasbourg, F-67000 Strasbourg, France*

<sup>6</sup>*Department of Physics and Astronomy, University of the Western Cape, Cape Town 7535, South Africa*

Accepted XXX. Received YYY; in original form ZZZ

## ABSTRACT

Utilizing the well-established Radial Tully-Fisher (RTF) relation observed in a ‘large’ (843) sample of local galaxies, we report the maximum allowed variance in the Hubble parameter,  $H_0$ . We estimate the total intrinsic scatter in the magnitude of the RTF relation(s) implementing a cosmological model-independent cosmographic expansion. We find that the maximum allowed local variation in our baseline analysis, using 4 RTF relations in the galaxy sample is  $\Delta H_0/H_0 \lesssim 3\%$  at a 95% C.L. significance. Which is implied form a constraint of  $\Delta H_0/H_0 = 0.54^{+1.32\%}_{-1.37\%}$  estimated at  $D_L \sim 10$  [Mpc]. Using only one ‘best-constrained’ radial bin we report a conservative 95% C.L. limit of  $\Delta H_0/H_0 \lesssim 4\%$ . Through our estimate of maximum variation, we propose a novel method to validate several late-time/local modifications put forth to alleviate the  $H_0$  tension. We find that within the range of the current galaxy sample redshift distribution  $10 \text{ [Mpc]} \leq D_L \leq 140 \text{ [Mpc]}$ , it is highly unlikely to obtain a variation of  $\Delta H_0/H_0 \sim 9\%$ , necessary to alleviate the  $H_0$ -tension. However, we also elaborate on the possible alternative inferences when the innermost radial bin is included in the analysis. Alongside the primary analysis of fitting the individual RTF relations independently, we propose and perform a joint analysis of the RTF relations useful to create a pseudo-standardizable sample of galaxies. We also test for the spatial variation of  $H_0$ , finding that the current samples’ galaxies distributed only in the southern hemisphere support the null hypothesis of isotropy, within the allowed noise levels.

**Key words:** (*cosmology*:) dark matter – galaxies – cosmological parameters

## 1 INTRODUCTION

To determine the value of the ‘‘Hubble Parameter’’:  $H(z)$  at different redshifts and in particular at present ( $H_0$ ) has become one of the most important and telling cosmological measurements. The well-established and increasingly prominent  $H_0$ -tension (Verde et al. 2019; Di Valentino et al. 2021) has paved the way to speculate several modifications to the concordance model of cosmology. At present, the significance of this discrepancy between the local model-independent Cepheid calibration-based supernovae yield  $H_0 = 73.04 \pm 1.04 \text{ km/s Mpc}^{-1}$  (Riess et al. 2021) and the Cosmic Microwave Background (CMB) based model-dependent ( $\Lambda$ CDM) indirect estimate  $H_0 = 67.66 \pm 0.49 \text{ km/s Mpc}^{-1}$  from the improved PR4 analysis in Tristram et al. (2023) is about  $\sim 5\sigma$ . In addition, the latter CMB estimate is corroborated by the Baryon Acoustic Oscillation data (Alam et al. 2021; du Mas des Bourboux et al. 2020; Zhao et al. 2019), providing  $H_0 = 67.81 \pm 0.38 \text{ km/s Mpc}^{-1}$  which only increases the

significance of the said tension. A more recent claim for a  $8.2\sigma$  tension was presented in Riess et al. (2024), addressing the cepheid crowding and their power-luminosity relation using JWST observations. Several reviews and discussions now provide a very good overview of the state of the tension (Abdalla et al. 2022; Riess 2019; Perivolaropoulos & Skara 2022; Schöneberg et al. 2021; Shah et al. 2021; Hu & Wang 2023; Efstathiou 2020; Freedman 2021; Knox & Millea 2020; Verde et al. 2023; Akarsu et al. 2024). Also, other local calibration techniques and measurements either provide a similar disagreement with the CMB estimate or at least do not yield immediate resolutions to explore (Pesce et al. 2020; de Jaeger et al. 2020; Schombert et al. 2020; Chen et al. 2019; Bonvin et al. 2017; Yuan et al. 2019; Blakeslee et al. 2021; Freedman et al. 2019; Wong et al. 2020; Jee et al. 2019; Shajib et al. 2020; Huang et al. 2019).

To resolve longstanding Hubble tension, several approaches have been proposed and explored ranging from modifications to early-universe physics (Poulin et al. 2021; Karwal & Kamionkowski 2016; Niedermann & Sloth 2021a,b; Zhao et al. 2017; de la Macorra et al. 2022; Jedamzik et al. 2021; Kreisch et al. 2020) to late-time/intermediate redshift physics

\* sharidas@sissa.it

† salucci@sissa.it

(Nygaard et al. 2023; Vattis et al. 2019; Akarsu et al. 2020; Blinov et al. 2020; Anchordoqui 2021; Haridasu & Viel 2020; Tutusaus et al. 2019; Solà et al. 2017; Tutusaus et al. 2023; Khosravi et al. 2019; Adil et al. 2024; Akarsu et al. 2023; Lapi et al. 2023), local Universe (Keenan et al. 2013; Whitbourn & Shanks 2014; Shanks et al. 2019; Hoscheit & Barger 2017; Colgáin et al. 2018; Luković et al. 2019; Cai et al. 2020; Alestas et al. 2021; Kenworthy et al. 2019), leading to extended discussions (Lee et al. 2023; Addison et al. 2018; Poulin 2020; Haridasu et al. 2021; Vagnozzi 2023; Bernal et al. 2021; Krishnan et al. 2021; Vagnozzi 2020; Gómez-Valent et al. 2024; Cao & Ratra 2023; Gómez-Valent et al. 2024). Alongside modifications to the physics of the Universe, possibilities that tension can arise due to systematics have been explored many times (e.g., Mortsell et al. 2022, 2021). Several techniques to study the possible resolutions of the Hubble tension under the least possible cosmological assumptions have also driven the need for model-independent techniques that have substantial significance in recent times, for example, (Liao et al. 2020; Pandey et al. 2020; Haridasu et al. 2018; Gómez-Valent 2018; Lemos et al. 2019; Lyu et al. 2020; Liu et al. 2023; Qi et al. 2023; Du et al. 2023; Li & Liao 2024, references therein).

In this context, the Tully-Fisher (Kourkchi et al. 2020) and the Baryonic Tully-Fisher (Kourkchi et al. 2022) relations, that have the advantage of possessing a clear physical justification (see Salucci et al. (1993); Salucci (2019)), have been utilized to estimate the local expansion rate, which has been consistent and at times providing even larger values of  $H_0$  with respect to the SH0ES estimate using SNe. These methods essentially highlight the necessity of alternate local estimations of  $H_0$  aiding immensely the discussion on  $H_0$ -tension and providing robust support to the Chephid-SNe-based local determination of the same. For a recent discussion see also Tully (2023). Along these lines, we intend to introduce the possibility of assessing the same using the Radial Tully-Fisher (**RTF**) relation for the first time. The RTF relation has been well established in Yegorova & Salucci (2007), following the discovery of a strong global relationship between the rotation velocities and the absolute magnitudes ( $M_I$ ) of the  $\sim 800$  nearby galaxies (Persic et al. 1996; Salucci 2019, and references therein). The RTF relation indicates that there exist independent radial Tully-Fisher-like relations at different galactocentric radii within spiral galaxies. In the current work, we take advantage of the RTF relation to obtain limits in the allowed variation of the Hubble rate within the local Universe  $z < 0.035$ , more precisely at the edge of the ‘Hubble-Flow’.

Several local ( $z < 0.1$ ) and ultra-local ( $z < 0.01$ ) (Alestas et al. (2021); Marra & Perivolaropoulos (2021); Desmond & Sakstein (2020); Desmond et al. (2019); Benevento et al. (2020); Banerjee et al. (2023)) physical resolutions and possible variations in the standardization of SNe (Alestas et al. (2022); Benisty (2023); Camarena & Marra (2023); Ruchika et al. (2023); Perivolaropoulos & Skara (2023)), have also been suggested to alleviate the  $H_0$ -tension, essentially relying on the fast transitions of physics in addition to the local void Keenan et al. (2013); Hoscheit & Barger (2017); Whitbourn & Shanks (2014) and extremely local ( $z < 0.015$ ) sharp transition of the dark energy equation of state Camarena & Marra (2019) etc. We anticipate the ability of the RTF relation to constrain proposed local modifications to the cosmological scenario by estimating the allowed variance in the local es-

timization of the Hubble parameter. We begin by reanalyzing the RTF relations presented in Persic et al. (1996) (here onwards PSS95) and Yegorova & Salucci (2007) (here onwards YS07) using improved Bayesian techniques. Given the nature of the empirical relations, we also propose a methodology improving the RTF relations by introducing a joint analysis to constrain the relations simultaneously, modeling a covariance among the individual relations.

The organization of the paper is as follows. After a brief introduction to the Radial Tully-Fisher relation in Section 2, in Section 2 we present the data. The cosmographic methodology and fitting of the RTF relations is described in Section 3. Finally, in Section 4, we present the results with an extended discussion.

## 2 RADIAL TULLY-FISHER RELATION

Adopting  $R_{\text{opt}}$ , the radius encompassing 83% of the total light of a Spiral Galaxy, as the reference size of its stellar disk, the radial Tully-Fisher relation is a family of TF-like relations observed in disk systems between the galaxy absolute Magnitude in a certain  $j$  band (e.g.  $M_I$ , the infrared band) and the rotational velocity  $V(R/R_{\text{opt}})$  measured at fixed normalized radii  $R/R_{\text{opt}}$ . These relations have been well established in YS07 with the help of the large sample of galaxies with good quality RCs from PSS95 and that of two additional samples with 86 and 81 high-quality RCs Courteau (1997); Vogt et al. (2004). In Fontaine et al. (2018) the RTF relationships have been established for a sample of 36 Dwarf Spirals and Irregulars.

The RTF relations, for a given magnitude  $M_j$ , are represented by a class of linear models,

$$M_j = a_n \times \log_{10}(V_n) + b_n \quad (1)$$

where the subscript  $n$  tags the radial bins in which the RTF is established. These bins are centered at the radii  $R_n$ , defined in terms of fractions of the optical radii. For the PSS95 sample, that we use in this work:  $R_n \equiv n/5R_{\text{opt}}$  and the bin width is  $1/5R_{\text{opt}}$ . Noticeably, the RTF has emerged also by adopting a smaller bin size, e.g.  $1/15R_{\text{opt}}$ , as in YS07 for the Courteau (1997); Vogt et al. (2004) samples of high-resolution RCs.

For the galaxies of the current Sample,  $V_n \equiv V(R_n)$  is the average value of the velocity data in each  $n^{\text{th}}$  bin,  $a_n$  and  $b_n$  are the slope and the intercept of the linear RTF relations found for the data belonging to the  $n^{\text{th}}$  bin<sup>1</sup>. Let us notice that in the constant  $b_n$  we can incorporate the term  $M_j(\infty) - M_j(R_n)$  which at a fixed  $n$  is equal in all galaxies, so that the L.H.S of Equation (1) can be interpreted as the aperture  $j$ -magnitude at the radius  $R_n$ , a quantity related to the mass in stars inside such radius.

It is worth demonstrating here that the RTF relationship with the features described above has a strong physical background as the originating TF one: it is a direct consequence of the fact that spiral galaxies are rotationally supported; their

<sup>1</sup> Since the surface luminosity density of the stellar disk  $I(R)$  is very similar in all spirals and it is represented by the well-known Freeman profile:  $I(R) \propto e^{-R/R_D}$ , the lengthscale  $R_{\text{opt}} = 3.2R_D$  describes the distribution of luminous matter for every spiral galaxy in the same consistent way.

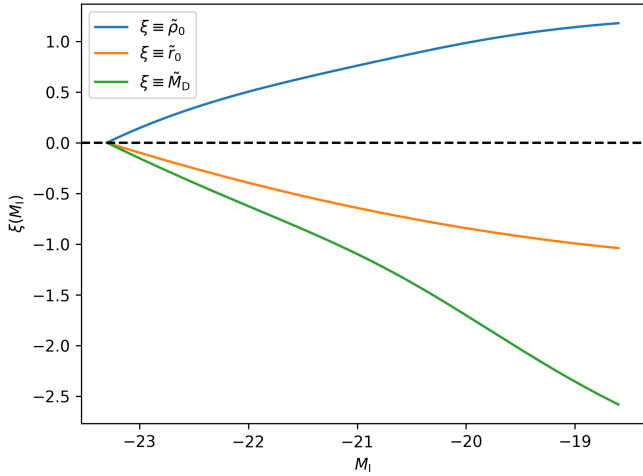


**Figure 1.** The parameters of the mass model of Spiral galaxies plotted as functions of the infrared Magnitude  $M_I$ .  $\bar{\rho}_0(M_I) = \rho_0(M_I)/(1.2 \times 10^{-25} \text{g/cm}^3)$  (blue),  $\bar{r}_0(M_I) = r_0(M_I)/(54 \text{kpc})$  (orange),  $\bar{M}_D(M_I) = M_D(M_I)/(4 \times 10^{11} M_\odot)$  (green).

circular velocities, at a radius  $R$  balance the gravitational attraction of the galaxy mass inside this radius  $R$ . Remarkably, in Spirals the mass distribution has universal features (see Salucci (2019)) and it includes 1) a Freeman stellar disk of mass  $M_D$  and length-scale  $R_D(M_I)$ , whose contribution to the circular velocity  $V(R)$  can be written as  $V_d(R/R_D; M_D)$  with the disk mass  $M_D$  as a free parameter of the mass model. 2) a cored dark matter halo whose contribution to  $V(R)$  can be written as  $V_h(R; \rho_0, r_0)$  (Salucci (2008)), with the central density  $\rho_0$  and the core radius  $r_0$  also as free parameters of the mass model. The resulting circular velocity model:

$$V_{\text{model}}(R) = [V_d^2(R/R_D; M_D) + V_h^2(R; \rho_0, r_0)]^{1/2} \quad (2)$$

successfully fits the circular velocities  $V(R)$  of the entire family of Spiral galaxies (PSS95; Salucci & Burkert (2000); Karukes & Salucci (2017); Salucci (2019)) provided that the above three free structural parameters become specific functions of the galaxy’s infrared magnitude  $M_I$

$$M_D(M_I); \quad r_0(M_I); \quad \rho_0(M_I), \quad (3)$$

shown in Figure 1 and given in PSS95 (see also Salucci & Burkert (2000)). By inserting the Equation (3) into Equation (2), one obtains that the latter becomes equivalent to the Equation (1) with the values of parameters given by Table 1 (see YS07 for the more details).

A further prediction of the physical origin of the RTF relationship is that in the innermost bin (i.e. for  $n = 1$ ) the relation should show a scatter sensibly larger than in the outer bins (i.e. for  $2 \leq n \leq 5$ ). This is due to the presence, in a good fraction of the objects of the sample, of a central stellar bulge that provides an important contribution to the mass enclosed in the innermost radius. The mass of this spheroid has a trend with that of the stellar disk, so that, the RTF continues to exist also for  $n = 1$ , but with a scatter larger than those at farther radii, not affected by the central bulge mass (see YS07). Let us also point out that, according to the above velocity model and directly supported by RCs data, we

have

$$V_{\text{model}}(n/5 R_{\text{opt}}, -23.) \simeq 10^{2.5} \text{ km/s} \quad (4)$$

for  $1 \leq n \leq 5$ . Thus the RTF relationship, that will be used here as a distance indicator, reflects the condition of the centrifugal equilibrium of a stellar disk embedded in a dark halo.

*Data:* In the current work, we utilize the same dataset that has been used to work out the ‘Universal rotational curve’ in PSS95 and later analyzed in Yegorova & Salucci (2007) to work out the Radial Tully Fisher. The dataset provides the magnitude of the galaxies in the ‘I’ band against the binned rotational velocity in each of the optical bins. In Figure 2 we show the redshift distribution of the galaxies which range between  $0.005 \leq z \leq 0.035$ , incidentally centered around  $z \sim 0.015$ , similar to the lower limit of  $z > 0.023$  usually taken to estimate the local value of  $H_0$  in SH0ES analysis Riess et al. (2016, 2018b), allowing the SNe to be in the ‘Hubble flow’. Notice that the peculiar motions of the galaxies in our sample, assumed to be 200 km/s, affect the determination of their redshift with an error, on average, of about  $\pm 0.08$  mag, i.e. a value smaller than the intrinsic scatter of the RTF relations, that amount to 0.12 – 0.25 mag; therefore, systematics that may arise in having not detailed these motions is small and likely washed out by the random uncertainty of the RTF relations. Moreover, in this work, the RTF distance indicator is used for tasks, whose complement does not require a good knowledge of the peculiar motions of galaxies.

In Figure 8 we show the RTFs for the different optical radii, alongside the best-fit linear relations, elaborated in Section 4. The distribution of these galaxies in the sky is shown in the Figure 3, which are a subset of those presented in the southern sky survey Mathewson et al. (1992). Here we show the distribution of the galaxies in Figure 3, in the J2000 system in contrast to the B1950 as was originally presented in Mathewson et al. (1992).

In summary, the Radial TF has been established in the process of investigating, in an innovative way (YS07), the mass distribution of Spirals: for the region inside their optical radii essentially providing evidence for: i) the presence of a massive Dark Component ii) the decrease of the DM/total matter fraction with increasing galaxy luminosity iii) a very shallow halo density profile iv) the presence of a central bulge component. *The role of the RTF thus far was therefore primarily intended to study dark matter properties in galaxies (e.g. Salucci (2019)). However, given the recent Hubble Tension, this tight and physically motivated Tully-Fisher-like relationship, even using the ‘original’ dataset can be a very efficient distance-indicator. The improvement, with respect to the TF is obvious, that the latter uses one circular velocity at a reference radius per galaxy, while the RTF exploits the full RC rotation curve inside the same optical radius of each galaxy.*

### 3 METHOD

We adopt the linear models shown in Equation (1) to perform regression to obtain the posteriors for each of the radial bins defined above in terms of the optical radius. In detail, firstly we perform a simple linear regression for each of the sub-samples split into the 6 bins with centers located at each of the first six 0.2 multiples of  $R_{\text{opt}}$ , wherein all the data points are assumed to be independent and no correlation is assumed

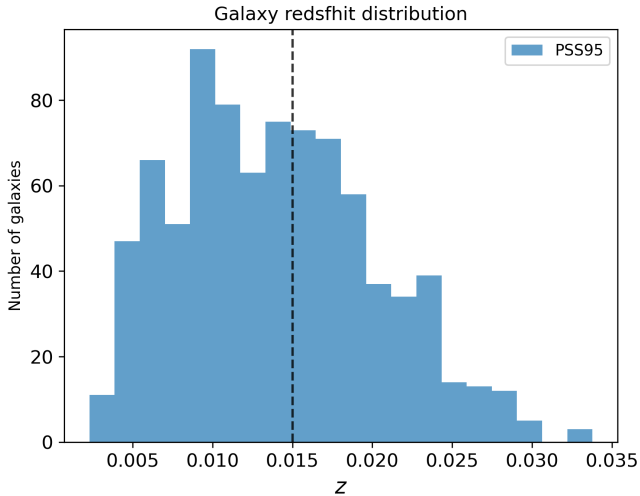


**Figure 2.** Redshift distribution of the PSS95 sample consisting of 489 galaxies below  $z < 0.015$  and 384 galaxies from  $z > 0.015$ .

in the analysis. For consistency, after performing the initial regression we exclude the data points that are more than  $3\sigma$  confidence level away from the posterior regressed line, to exclude the outliers. However, we also note that this exclusion of the outliers does not significantly affect the final inferences drawn from the analysis. The analysis requires 3 parameters for each of the RTF relations taking into account the slope, intercept, and intrinsic scatter  $\{a_n, b_n, \sigma_n\}$ , amounting to a total of 18 total parameters to fit the 6 optical bins considered in the current dataset. Note that throughout the analysis we assume and fix a fiducial value of  $H_0 = 70 \text{ km/s Mpc}^{-1}$  and  $q_0 = -0.55$ . Varying the value of  $H_0$  within the current analysis with a simple cosmographic background, presented in the next section, only amounts to an overall shift of all RTF relations with no implication for the shape of the RTF relations. This remains a valid assumption given no significant empirical indications to go beyond the linear relations.

### 3.1 Cosmography

To utilize the given galaxy samples to estimate the maximum allowed variance in the Hubble parameter we implement a simple cosmographic approach to model the luminosity distance as,

$$D_L(z) = \frac{c}{H_0} \times \left[ z + \frac{1}{2}(1 - q_0)z^2 \right], \quad (5)$$

where  $H_0$  is the current expansion rate and  $q_0$  is the deceleration parameter. The distance modulus can now be written as the difference between the apparent magnitude and the absolute magnitude,

$$m_I - M_I = 25 + 5 \log_{10} (D_L(z) [\text{Mpc}]), \quad (6)$$

wherein we utilise the recession velocity ( $V_{\text{rec}}$ ) of each of the galaxies to obtain the redshift  $z = V_{\text{rec}}/c$ . Note that the above equation can further be approximated, taking only the first-order term in Equation (5) into account,

$$m_I - M_I = 25 + 5 \log_{10} (V_{\text{rec}}/H_0). \quad (7)$$

Finally, given the assumed cosmography to obtain the absolute magnitude of the data points and the posteriors of linear regression models obtained through the fitting relation Equation (1) we construct the residuals of the absolute magnitude as a function of the redshift. The redshift of the galaxies is consistently obtained utilizing the recession velocity of the galaxies, as described earlier. Also, one could equivalently present the same in terms of the luminosity distance of the galaxies instead of redshift, which we present as the final result (elaborated in Section 4).

### 3.2 Joint analysis

The methodology described so far follows YS07 and constrains each of the RTF relations individually. While we utilize the same as a first step, in this work we also introduce a method to perform joint analysis and simultaneously constrain the RTF relations. As can be seen in the Figure 8 and also in Figure 2. of YS07, all the individual RTF relations at each optical bin converge at a ‘pivot’ that remains to be a fixed point depending only on the value of  $H_0$  assumed in the conversion of the observed apparent magnitudes to the absolute magnitude  $M_I$  through Equation (5), and the distance modulus expression. As shown in Section 2 we remind that the mass model of spiral galaxies at all radii is observationally unrelated to the RTF, implying the existence of this pivot quantity.

This, in turn, modifies the individual RFT description in Equation (1) with a pivot as,

$$M_j - M_I^{\text{Pivot}} = a_n \times (\log_{10}(V_n) - \log_{10}(V^{\text{Pivot}})) \quad (8)$$

where the pivot is given by  $\{M_I^{\text{Pivot}}, \log_{10}(V^{\text{Pivot}})\}$  and the corresponding slopes  $a_n$  of the individual relations. In contrast to the total of 18 parameters describing the 6 independent relations, within the joint analysis setup, we have 14 parameters: 12 describing the slopes and intrinsic scatter of the six relations, and two fixing the pivot.

Finally, the likelihood of the individual linear regression analysis within each of the radial bins  $n$  can be written as,

$$-2 \log(\mathcal{L}) = \sum^{N_{\text{gal}}^n} \left[ \frac{(M_I^{\text{obs}} - M_I^{\text{theo}}(V_n))^2}{\sigma_n^2} \right], \quad (9)$$

where the  $M_I^{\text{obs}}$  is constructed using Equation (6), while the  $M_I^{\text{theo}}(V_n)$  assume the form in Equation (1), with the free parameters  $\Theta \equiv \{a_n, b_n\}$ , and  $\sigma_n$  is a free parameter assessing the intrinsic scatter of the data. Here  $N_{\text{gal}}^n$  is the number of galaxies with rotational curve velocities in  $n^{\text{th}}$  radial bin. Similarly, the likelihood for the joint analysis is written as,

$$-2 \log(\mathcal{L}) = \sum^n \sum^{N_{\text{gal}}^n} \left[ \frac{(M_I^{\text{obs}} - M_I^{\text{theo}}(V_n))^2}{\sigma_n^2} \right], \quad (10)$$

wherein a summation over the radial bins  $n$  is included and the  $M_I^{\text{theo}}(V_n)$  is given by Equation (8), with free parameters  $\Theta \equiv \{M_I^{\text{Pivot}}, \log_{10}(V^{\text{Pivot}}), \mathbf{a}_n\}$  amounting to a total of 14 parameters as described earlier. Note that one could include an additional parameter  $\tau$  as a penalty term  $\log(\tau + \sigma_n^2)$  to the

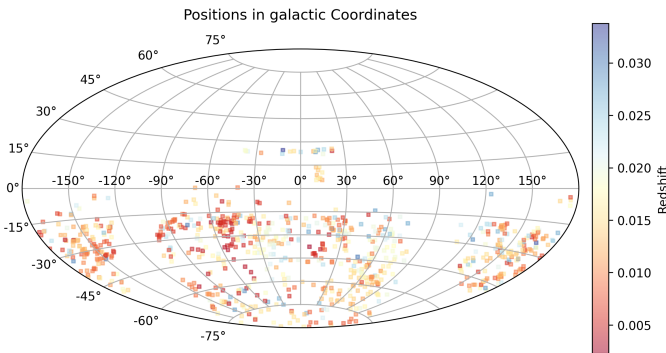


**Figure 3.** Distribution of the galaxies utilized in the current analysis. The vertical color bar shows the redshift distribution of the galaxies.

total likelihood. This would describe a degeneracy/covariance between the 6 RTF relations, to be more conservative and validate the utility of the magnitude used in RTF relation at each optical bin. In other words, the parameter  $\tau$  takes into account the variability between the individual RTF relations, enforcing a covariance amongst them. However, note that this does not curtail the use of individual RTF relations to assess the Hubble variance, but aids an opportunity to construct a ‘standardizable’ sample of galaxies that follow a scaling relation, and can be utilized for additional distance ladder analysis, which we intend to perform as an independent full-fledged analysis. As we shall elaborate later in the Section 4.3, we do not find strong correlations between individual radial bins, and therefore we leave this assessment to a future analysis.

To perform the fully Bayesian analysis we utilize the publicly available `emcee`<sup>2</sup> package (Foreman-Mackey et al. 2013), implementing an affine-invariant ensemble sampler. We analyse the generated MCMC samples using `corner` and/or `Get-Dist`<sup>3</sup> Lewis (2019) packages.

### 3.3 Isotropy of the local universe

Given the availability of the galaxy positions Mathewson et al. (1992), we also estimate the isotropy and the subsequent variance in the sky of the current sample. Note that the current sample only covers the southern sky and is not an isotropic survey allowing us to assess the overall isotropy being biased on large scales. Therefore, we estimate the overall noise level that would be expected in an isotropic universe, utilizing the bootstrapping methodology presented in Soltis et al. (2021). In this method, the positions of the galaxies are permuted amongst themselves essentially rearranging under the assumption that in an isotropic universe, the galaxies could have been observed in any of the given positions within the sky coverage of the survey. In Soltis et al. (2021), the residuals of the supernovae magnitudes within the MCMC fitting are utilized as the indicators for the noise levels. Similarly, we utilize

$$r_i = \frac{M_{I,i}^{\text{theory}} - M_{I,i}^{\text{data}}}{\sigma_{M_{I,i}^{\text{data}}}} \quad (11)$$

as the indicators for the same, where  $i$  iterates over the number of galaxies. The assumption of these residuals as an indicator is valid as we do not intend to estimate the actual isotropy itself but rather the noise level present within the distribution of the galaxies and contrast against the observed positions of the galaxies. Using these residuals in the sky we estimate the clustering of the galaxies by estimating the angular power spectrum  $C_l$ , the range of which depends on the assumption of the NSIDE<sup>4</sup> of the constructed maps. In this analysis, we present our results for NSIDE = 16, while we validate that a different assumption does not change our inference substantially. For each of the galaxies, we take the total residual obtained from all the available optical bins and then an average value of these residuals for all the galaxies falling within each pixel of the map. We perform 1000 bootstrap steps for every set of the model parameters within the MCMC chain that are iterated 1000 times, yielding a total of a million steps taking into account uncertainty in the RTF relations. It is important to note that the linear regression of the RTF relations described in the earlier sections is performed assuming no uncertainty ( $\sigma_{M_{I,i}^{\text{data}}} = 0$ )<sup>5</sup> on the  $M_{I,i}^{\text{data}}$ . However, in estimating the noise level associated with the statistical isotropy, we assume the reasonable conservative value of  $\sigma_{M_{I,i}^{\text{data}}} = 0.075$  (Mathewson et al. 1992) for the photometric measurements errors.

## 4 RESULTS

We begin by re-analyzing the PSS95 sample containing 6 different radial bins ( $R_{\text{opt}}$ ). The results obtained for the fitting of the individual RTFs are summarised in Table 1 for completeness, and are consistent in comparison to those presented in YS07 (see Table A1. therein). In the current Bayesian formalism the mean values of the scatter are mildly larger along with associated uncertainty. Following this to assess the redshift variation, as a preliminary step, we split the galaxy sample into two redshift bins performing the linear regression in each of the radial optical bins. In Figure 4 we show the intrinsic scatter as obtained for each of the radial bins when the regression is performed with only samples  $z \leq 0.015$  and  $z \geq 0.015$  are considered independently. We find a very good consistency between the intrinsic scatter estimated for the galaxies with the redshift cut which asserts that a redshift-dependent analysis would not be biased due to the variation in the galaxy dataset over redshift. This allows us to estimate the variance of the Hubble parameter as a function of redshift and, consequently luminosity distance. For the innermost optical bin  $0.2 R_{\text{opt}}$ , we find the intrinsic scatter is mildly larger for  $z < 0.015$ , however consistent within  $2\sigma$ .

<sup>4</sup> The NSIDE fixes the resolution of the maps.

<sup>5</sup> The anticipated intrinsic scatter of the RTF relations is much larger than error on the magnitudes of the galaxies and the inclusion of  $\sigma_{M_{I,i}^{\text{data}}}$  error would fall completely within the prior. For this reason, we remain with fitting eh RTF relations to estimate the maximum scatter.

<sup>2</sup> <http://dfm.io/emcee/current/>

<sup>3</sup> <https://getdist.readthedocs.io/>

**Table 1.** We show the posteriors, including the 68% C.L. limits for the linear regression parameters, performed for each of the radial bins shown in Figure 8. The first column is the radial bins and the next three columns present the results obtained by fitting the RTFs individually. In columns 4 and 5 we show the results obtained in the joint analysis. In the last column, we show the number of data points utilized in the regression in each bin. All constraints reported here are obtained assuming  $H_0 = 70 \text{ km/s Mpc}^{-1}$ .

$R_n [R_{\text{opt}}]$	$b_n$	$a_n$	$\sigma_n^{\text{int}}$	Joint		$N_D$
				$a_n$	$\sigma_n^{\text{int}}$	
0.2	$-11.98 \pm 0.11$	$-4.67 \pm 0.06$	$0.402 \pm 0.011$	$-4.62 \pm 0.04$	$0.370 \pm 0.012$	749
0.4	$-8.18 \pm 0.07$	$-6.15 \pm 0.03$	$0.191 \pm 0.005$	$-6.16 \pm 0.03$	$0.108 \pm 0.010$	793
0.6	$-5.78 \pm 0.06$	$-7.11 \pm 0.03$	$0.148 \pm 0.004$	$-7.11 \pm 0.02$	$0.013 \pm 0.009$	799
0.8	$-4.21 \pm 0.09$	$-7.72 \pm 0.04$	$0.173 \pm 0.005$	$-7.76 \pm 0.03$	$0.068 \pm 0.016$	663
1.0	$-3.02 \pm 0.15$	$-8.20 \pm 0.07$	$0.214 \pm 0.007$	$-8.18 \pm 0.04$	$0.145 \pm 0.012$	454
1.2	$-2.06 \pm 0.26$	$-8.61 \pm 0.12$	$0.262 \pm 0.013$	$-8.44 \pm 0.06$	$0.157 \pm 0.004$	231

Given the large intrinsic scatter in this bin, mostly due to the random presence of a not-negligible compact bulge component in our galaxies, it is difficult to estimate the rotational velocity very accurately along the lines of the bulge-free Equation (2). Therefore, we exclude this bin in our baseline analysis when estimating the overall variance<sup>6</sup>. We also exclude the outermost bin, owing to the low sample density having only  $\sim 230$  data points, and the fact that the accuracy in measuring the rotational velocity from the  $H_\alpha$  line is low at the outskirts of the spiral galaxies. Nevertheless, we retain the advantage of utilizing 4 independent radial bins to estimate the overall scatter. From here onwards we remain with 4 optical bins as our ‘baseline’ dataset to present our main results to evaluate the cosmological variance of the Hubble parameter. However, we do comment on the implications of utilizing these two bins as they present interesting scenarios in assessing the Hubble variance. The  $0.6 R_{\text{opt}}$  bin having the least scatter<sup>7</sup> and being best constrained RTF, is a conservative estimate to which we compare the joint constraint in our analysis.

Having the Tully-Fisher relation fitted in each of the bins, and establishing that the dataset is suitable for the assessment of redshift variation, we now evaluate the residual of the absolute magnitude, w.r.t the fitted linear regression. We conservatively anticipate the intrinsic scatter and hence the absolute residual,  $\Delta M_I$  to account for cosmological variation which can be converted to the variance in the expansion rate as given by Section 4, also considering the uncertainty of the RTF relations<sup>8</sup>. Note that we also exclude the galaxies that are more than  $3\sigma$  away from the residuals deeming them to be outliers<sup>9</sup>. Following Equation (7), we now trans-

<sup>6</sup> The effect of the bulge in RTF is discussed in YS07.

<sup>7</sup> Also for the RTFs emerging in the Vogt et al. (2004); Courteau (1997) samples.

<sup>8</sup> We validate that including the uncertainty of the RTF relation itself makes very little difference to our final estimates, since the intrinsic scatter much larger in comparison.

<sup>9</sup> We find only about 5-10 galaxies per radial bin to satisfy the outlier condition, which however could be an important assessment as the lower  $D_L < 20$  [Mpc] and  $D_L > 120$  [Mpc] distance bins with a low number of galaxies can get mildly affected. We also validate

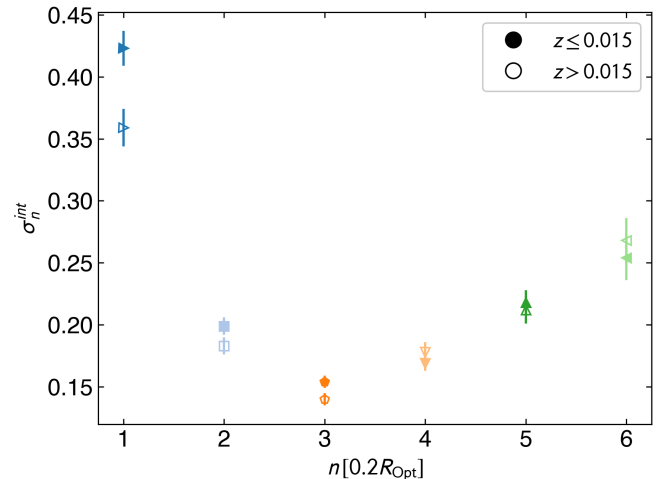


**Figure 4.** The intrinsic scatter and the  $1\sigma$  error, within each of the radial bins, however, split at redshift  $z \sim 0.015$  to assess the variation in the different redshift bins.

late the average dispersion in the residual of RTF relation as the maximum possible variance in the value of  $H_0$  as,

$$\frac{\Delta H_0}{H_0}(z) = \frac{\ln 10}{5} \overline{\Delta M}(z). \quad (12)$$

Which is now recast as the redshift evolution of the allowed fractional variation in the Hubble parameter as shown in Figure 5, by binning the residuals appropriately. In this figure, we show the mean of the residuals for the best-fit RTF relations and the uncertainty on the same, estimated as the standard error. We present the residuals in all the radial bins while assessing the corresponding cosmological distance ( $D_L$ ) using Equation (7), assuming that the redshift is given by the recession velocity ( $V_{\text{rec}}$ ) as  $z = V_{\text{rec}}/c$ . We then compute the average variation of the  $\Delta M_I$  in each of the redshift/distance bins

that this step does not make a significant difference to our final inference.

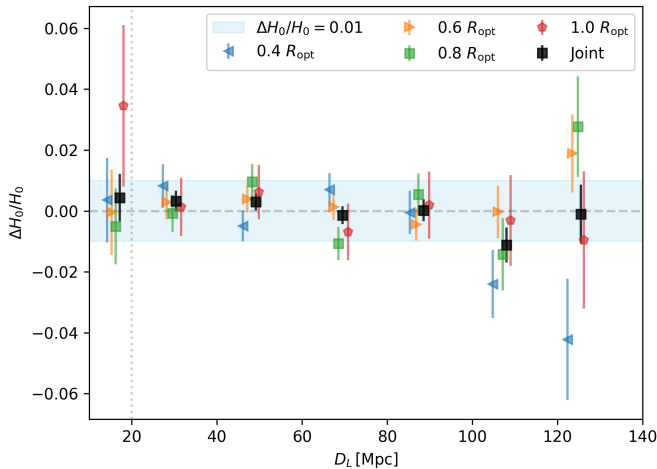


**Figure 5.** The variation in the Hubble parameter utilizing all 5 radial optical bins simultaneously. The data points have been slightly shifted in the x-axis for better visualization.

split accordingly. Needless to say, the difference in the number of data points (galaxies) in each bin is reflected in the uncertainty estimated as standard error  $\sigma_{\Delta H_0/H_0} = \sigma_{\Delta H_0/H_0} / \sqrt{n_i}$ , where  $n_i$  is the number of data points (galaxies) in each redshift bin. As we have already mentioned, each of the RTF relations fitted in the 6 optical bins can be considered independent relations with no correlations whatsoever. Therefore, in the joint analysis of all the radial bins  $R_n[R_{\text{opt}}]$  considered, we follow the same procedure considering each velocity measurement in each radial bin as an independent data point. In Figure 5 we show the variation in the residuals of absolute magnitudes of the galaxies, as a function of the luminosity distance, wherein we have binned the luminosity distance into linear bins of size  $\Delta D_L = 20$  [Mpc].

As can be seen in Figure 5, we find that there is no discernible redshift evolution of the Hubble variance, always consistent within  $\sim 5\%$ , suggesting no variation in the current redshift range. We find that the joint constraint to sub percent precision always being consistent with  $\Delta H_0/H_0 = 0$  within the  $\sigma_{\Delta H_0/H_0}$ . For the  $0.4 R_{\text{opt}}$  we find the maximum variation to be  $\sim 10\%$  comparing the data point at  $\sim 120$  Mpc with the innermost data point at  $\sim 17$  Mpc. Similarly, the  $1.0 R_{\text{opt}}$  also shows a mild increase in the variance in the innermost distance bin. However, this trend is not immediately corroborated in the  $0.6 R_{\text{opt}}$  and  $0.8 R_{\text{opt}}$  radial bins, which are the better-constrained RTF relations showing no statistically significant trend. This is also reflected in the joint constraint shown as black data points in Figure 5. Moreover, there seems to be a mild decrease in the values of  $\Delta H_0/H_0$ , especially around the  $D_L = 100$  [Mpc] range, however, completely consistent within the  $\sim 2\sigma$  C.L. for  $\Delta H_0/H_0 = 0$ .

We contrast our results for the uncertainty in the evolution of the Hubble parameter against the constraints obtained from the Supernovae datasets in the local universe. Although the current galaxy dataset utilized in this work only extends up to  $D_L \sim 140$  [Mpc], we confirm that within this range such an under-density is not suggested by utilizing the RTF

relation. This is in agreement with the earlier analysis in Kenworthy et al. (2019); Luković et al. (2019); Camarena & Marra (2019) using SNe datasets. An under density of size  $\sim 300$  [Mpc] Hoscheit & Barger (2017) and a similar less significant local hole of  $\sim 150$  [Mpc] Shanks et al. (2019); Whitbourn & Shanks (2014) were proposed as possibilities to alleviate the Hubble tension by modifying the current expansion rate measured by the local supernovae. To comment on which one would need to extend the current sample to a higher redshift range Stone et al. (2022) (left for a future investigation). Within the redshift range of the current dataset, we find that local  $z < 0.01$  sharp phantom transitions as proposed in Alestas et al. (2021) are less likely. Similarly, sharp transitions in the gravitational constant ( $G_N$ ) local/ultra-local universe Marra & Perivolaropoulos (2021); Alestas et al. (2022); Benisty (2023); Camarena & Marra (2023); Perivolaropoulos & Skara (2023) and local modifications Ruchika et al. (2023) have also been suggested as a possibility for the discrepancy in the locally measured  $H_0$  and the value inferred from the CMB assuming model, which our results so far do not immediately suggest. In other words, we notice that in the current linear binning of distance, the innermost constraint obtained at  $D_L \sim 17$  [Mpc] is completely consistent with no evolution of the  $\Delta H_0/H_0$ . This constraint is also consistent with the second bin centered at  $D_L \sim 30$  [Mpc]. As can be seen in Figure 5, our conservative inference using only the radial bin  $0.6 R_{\text{opt}}$  is completely consistent with the joint constraint of the 4 considered so far. However, please refer also to the Section 4.1 and appendix A for mild yet alternate perspectives mostly arising due to different binning schemes and the inclusion of inner and outermost radial bins.

#### 4.1 Inclusion of the innermost bin and alternate binning

In this section, we present the results as obtained when the innermost  $0.2 R_{\text{opt}}$  and outer bins  $1.2 R_{\text{opt}}$  are also included in the analysis. We also change the binning scheme of the distances to test for the validity of including the innermost bin while accommodating variations also on the closet and the farther-distance bins. In Figure 6, the black data points show the joint constraint taking into account all the  $R_{\text{opt}}$  bins and increasing the number of distance bins in contrast to the earlier results in Figure 5. As one can immediately notice the joint constraints show a trend of increasing  $\Delta H_0/H_0$  for lower distances. This change is completely driven by the  $0.2 R_{\text{opt}}$  bin alone, while the outermost bin, having only 231 data points, makes minimal difference to joint constraints.

We show results for finer binning in distances with  $\Delta D_L \sim 5$  [Mpc], at the expense of precision in each bin to evaluate the overall shape of  $\Delta H_0/H_0(z)$ . We find that the  $0.2 R_{\text{opt}}$  strongly influences the joint constraint, showing significant evidence for a possible cosmological signature for an increasing value of the Hubble parameter in the ‘ultra-local’ ( $D_L \lesssim 30$  [Mpc]) regime. Needless to say, to make this inference is heavily reliant on the binning scheme, as the closer distance bins tend to have very few galaxies providing the jump we notice therein. For instance, within the joint analysis of all the radial bins (black data points in Figure 6), the first bin centered at  $D_L \sim 14.4$  [Mpc] and the last bin at  $D_L \sim 133.2$  [Mpc] contain merely 5 and 3, galaxies, respectively. In this case the difference in the bins is  $\Delta H_0/H_0 \sim 0.1$ , which is about  $\sim 10\%$  variation in the value of absolute  $H_0$ .

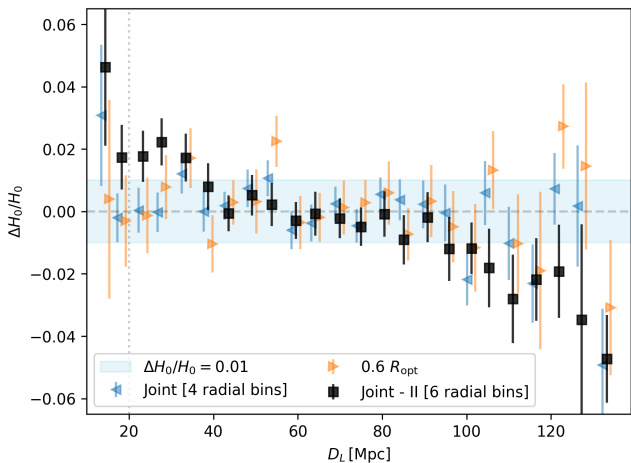


**Figure 6.** Same as Figure 5 with different binning schemes and inclusion of the innermost radial  $0.2 R_{\text{opt}}$  bin. Black data points show the results using the same binning as in Figure 5.

Note that this level of variation difference could play a significant role in explaining the  $H_0$ -tension which is  $\sim 8\%$  difference between the local and the CMB estimates. We also show and validate that the  $0.6 R_{\text{opt}}$  radial bin shows no such behavior using the finer bins, with mildly increasing scatter of the mean at larger distances.

The initial consideration to leave this bin out of the joint analysis is because the central bulge in the spiral galaxies does not allow one to measure the rotational velocity accurately. Therefore, the validity of the redshift-dependent behavior of  $\Delta H_0/H_0$  we find in Figure 6, is subject to the confidence in the rotational velocities measured in the innermost regions of the spiral galaxies. In YS07, the authors provide a relationship (see Eq.14 therein) between the slopes of the individual RTFs and the optical radii, indicating the validity of the RTFs also in the bulge of the galaxies. This is once again an empirical relation that is observed and fitted in the current galaxy sample and it is also shown that this expectation is consistent when considering the two other galaxy samples they have tested. However, in a conservative approach, we tend to remain with our 4-bin analysis or equivalently 5 bins including the outermost radial bin, not claiming significant evidence for a redshift evolution of  $\Delta H_0/H_0$ . This variation has to be validated in larger galaxy samples with better estimations of the central rotational velocities and would be untimely to claim a possible detection of local variation in  $H_0$  using the current dataset alone. We leave this for a future investigation using the PROBES (Arora et al. 2021) dataset. However, it is interesting to note that the innermost bin carries significant statistics being able to sway the joint analysis using all 6 bins.

#### 4.2 Smoothing the binned variance

While we have so far presented our results by binning the galaxies in distance, we now implement a simple smoothing of the scatter using the locally weighted scatter regression of the

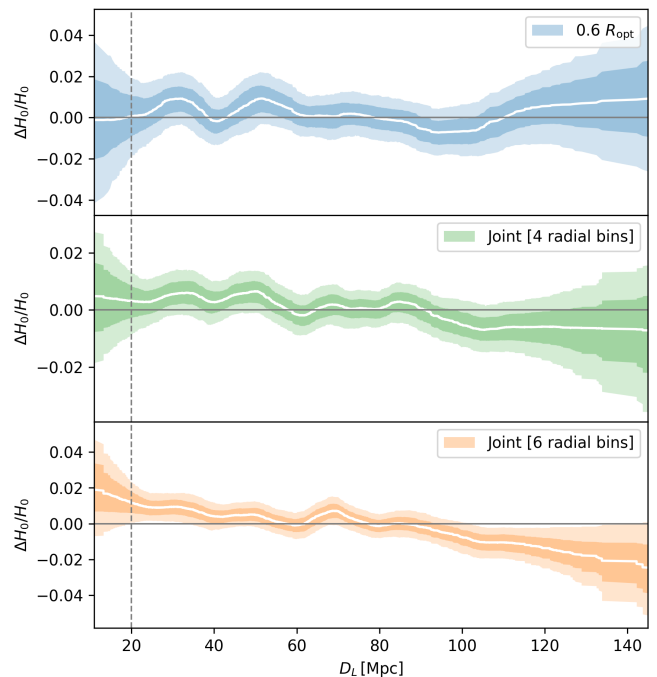


**Figure 7.** *Top:* We show the  $1\sigma$  and  $2\sigma$  C.L. of the fit to the  $0.6 R_{\text{opt}}$  bin. *Center:* Similar to the top panel, for the baseline Joint analysis with the 4 radial bins and for comparison, we also show the results from all the 6 radial bins in the *Bottom* panel.

scatter (LOWESS<sup>10</sup>) obtained in the  $\Delta H_0/H_0$  vs.  $D_L$  plane. This technique has been utilized in various contexts in Montiel et al. (2014); Escamilla-Rivera et al. (2021); Bernardo & Levi Said (2021); Fernández-Hernández et al. (2019). We implement this essentially to represent the variation in  $\Delta H_0/H_0$  as a smooth function of  $D_L$  and simultaneously obtain the uncertainty on the estimated variance. Similar to the binning schemes where we have to assume the size of the  $\Delta D_L$ , here we need to assume a fraction ( $f \in \{0, 1\}$ ) of the data that will be considered to obtain the locally weighted least squares fit. Higher values of this fraction will consider a larger number of data points eventually providing a smoother reconstruction of the scatter plot. This technique while being ‘non-parametric’ also allows one to obtain the uncertainty region by simply bootstrapping on the scatter points. We utilize this method to present our final constraints on the  $\Delta H_0/H_0$  as our main result in terms of uncertainty and the upper limits.

We show the results of the LOWESS smoothing in Figure 7 for three different scenarios: using only the central  $0.6 R_{\text{opt}}$  bin alone, our baseline analysis with 4 radial bins and all 6 radial bins included. Here we have utilized  $f = 0.2$ , while we have tested the results also with the larger fractions. We show a comparison of the constraints and 95% upper limits on  $\Delta H_0/H_0$  in Table 2, for  $f = 0.2$  and  $f = 0.5$  fractions. Using

<sup>10</sup> Locally weighted scatter plot smoothing (LOWESS) (Cleveland & Devlin 1988; Cleveland 1979). We utilize the publicly available `statsmodels` package Seabold & Perktold (2010) for this purpose. A simple example of how to perform the same can be found here. Please see also Cook & Weisberg (1999); Fox (2008, 2024); Andersen (2009) for more details.



Bins	$\Delta H_0/H_0[\%]$			
	$f = 0.2$		$f = 0.5$	
	68% C.L.	< 95% C.L.	68% C.L.	< 95% C.L.
$0.6R_{\text{opt}}$	$-0.11^{+2.06}_{-1.96}$	3.90	$0.35^{+1.04}_{-1.18}$	2.64
4 bins	$0.54^{+1.32}_{-1.37}$	2.98	$0.34^{+0.63}_{-0.74}$	1.74
6 bins	$2.08^{+1.65}_{-1.39}$	5.17	$1.45^{+0.72}_{-0.69}$	2.79

**Table 2.** We show the 95% C.L. upper limits on the  $\Delta H_0/H_0[\%]$ , for the two cases of the fraction of data utilized in the analysis. The  $f = 0.2$  column corresponds to the uncertainty regions presented in Figure 7.

lower fractions ( $f < 0.1$ ) tends to provide very few galaxies for each locally weighted regression, essentially mimicking the scatter with very large mean squared errors. Note that traditionally the fraction of data to be utilized is optimized for the least possible mean square error through cross-validation techniques (Montiel et al. 2014, see references therein). In our case, this typically corresponds to the larger values of  $f$ , as can be seen in the last column of Table 2. Therefore we remain with the conservative  $f = 0.2$  fraction of data to present the limits expected on  $\Delta H_0/H_0$ .

As shown in Table 2, using only the  $0.6R_{\text{opt}}$  bin we find  $\Delta H_0/H_0 [\%] = -0.11^{+2.06}_{-1.96}$  with a 95% C.L. upper limit of  $\Delta H_0/H_0 < 3.9\%$ . We interpret this limit as a conservative upper limit on the allowed local variation on  $H_0$ . Note that this limit is estimated at a distance  $D_L \sim 10$  [Mpc]. Similarly, we find the upper limit at 95% C.L. limits is  $\Delta H_0/H_0 \lesssim 3\%$  which we infer as our best estimate. Needless to say, these limits are tighter when we utilize  $f = 0.5$ , as can be seen in the last two columns of Table 2. We also find that similar features are reconstructed in both these cases, validating the use of 4 bins as our baseline dataset. We notice a mild dip at  $D_L \sim 100$  [Mpc] and a rise at  $D_L \sim 30$  [Mpc], albeit with a low significance of  $\sim 1\sigma$ . Finally, with the inclusion of the innermost radial bin, the redshift dependence of  $\Delta H_0/H_0$  is evident as depicted in the bottom panel of Figure 7. This also translates to a detection of  $\Delta H_0/H_0 > 0$  at C.L. of  $\sim 1\sigma$  ( $f = 0.2$ ) and  $\sim 2\sigma$  ( $f = 0.5$ ).

### 4.3 Joint analysis

As anticipated in Section 3, we perform the joint analysis of the RTFs considering the pivot point as parameters of the fit and individual slopes and intrinsic scatters for each of the RTFs as free parameters. To validate this assumption, we first perform a rolling regression<sup>11</sup> analysis where no binning is considered but all the data points from all the bins are simultaneously fitted assuming a gradually changing slope. Wherein we recover that all the regression lines pass through the pivot point, without an explicit assumption of the same. In Figure 8, we show the RTF relations fitted against data in this approach. As can be seen in Figure 8 and also in

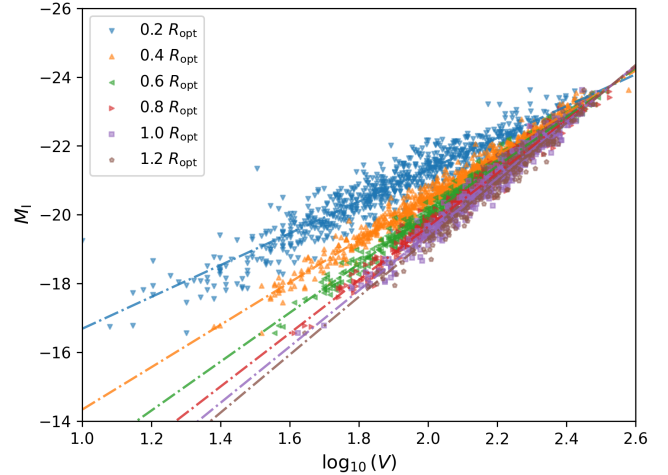


**Figure 8.** Scatter corresponding to the RTF relations in the 6 bins of  $R_{\text{opt}}$  taken from PSS95 and the linear best-fits obtained from our joint analysis assuming  $H_0 = 70$  km/s Mpc<sup>-1</sup>.

Table 1 we find a very good agreement with the scenario when performing individual fits, especially contrasting the slope of the RTF relations. We obtain the following constraints for the pivot parameters,

$$\begin{aligned} M_I^{\text{Pivot}} &= -23.830 \pm 0.066, \\ \log_{10}(V^{\text{Pivot}}) &= 2.526 \pm 0.009. \end{aligned}$$

The estimates of the intrinsic scatter and their uncertainty, are at times lower than those obtained in the individual fits. This is clearly because a fraction of the uncertainty is now attributed to the estimation of the pivot, and reduction in the overall degrees of freedom, in the joint analysis. In Figure B2, we show the correlations between the posteriors of the slopes and the pivot point. As expected there exists a strong anti-correlation between the parameters  $\log_{10}(V^{\text{Pivot}})$  and  $M_I^{\text{Pivot}}$ . The slopes of the individual RTF relations are correlated with the coordinates of the pivot point, ranging from anti-correlations for the inner-most  $0.2R_{\text{opt}}$  RTF to positive correlation for the outer-most  $1.2R_{\text{opt}}$  RTF. In this context, it is interesting to note that the slope of  $0.6R_{\text{opt}}$  RTF is almost completely uncorrelated to the pivot point and shows only mild correlations with the slopes of the other RTFs. This also validates the existence of a very well-constrained individual RTF relation in this optical bin.

We show the complete contour plot of all the parameters of the MCMC analysis in Figure B3, for brevity in the main text. The analysis so far has been performed assuming  $H_0 = 70$  km/s Mpc<sup>-1</sup>, which is necessary to estimate the distances to galaxies. In Figure B1 we show the comparison the posteriors when the  $H_0$  is assumed differently, being either 67 km/s Mpc<sup>-1</sup> Aghanim et al. (2020) or 73 km/s Mpc<sup>-1</sup> Riess et al. (2021). As anticipated the magnitude of the pivot point is strongly affected by the assumption, while the velocity remains completely unchanged. Also indicating that not assuming a particular value of  $H_0$  mainly affects the overall

<sup>11</sup> We use PyMC Wiecki (Wiecki); Salvatier et al. (2016) for this purpose.

scale of the RTF relations and not necessarily the shape of individual relations. However, the redshift dependence of the data can be affected by the assumption of underlying cosmology and tentatively this in turn can allow one to use the current dataset to constrain the value of  $H_0$ . We intend to present this in the second installment of this pilot analysis, utilizing also the necessary local distance calibrators.

#### 4.4 Variance on the sky

As yet we have only estimated the variation of the Hubble parameter as a function of redshift, however now we turn to the anisotropy in the estimate of the  $H_0$  on the sky. For this purpose, we utilize the method presented in Soltis et al. (2021), wherein the angular clustering of the Supernovae sample Riess et al. (2018a); Scolnic et al. (2018) was estimated and a percent level spatial variation in the Hubble constant was reported. Following this methodology, we compute the spatial clustering of the galaxies in the current PSS95 sample, which is a collection of galaxies in the southern hemisphere as shown in Figure 3. Note however, that in contrast to the SNe datasets that extend all the way to  $z \lesssim 2.3$ , our dataset of local galaxies is restricted to  $z \leq 0.03$ , allowing us to test explicitly for the local anisotropy.

In Figure 9, we show the power spectrum of the spatial clustering of the galaxies. The black data points and the associated uncertainties represent the clustering of the galaxies varying on the parameters of the RTF relations as fitted in the MCMC analysis Figure B3. The blue-shaded region shows the 68% C.L. uncertainty on the noise level associated with the statistical variation expected in an isotropic universe, given the observed positions of the current galaxies. As can be seen the angular power spectrum of distribution of the galaxies in the current catalog is perfectly consistent within the  $\lesssim 1\sigma$  level, with the isotropic expectation, indicating no signal for anisotropy. The current sample only occupies the southern hemisphere, which is reflected in the data and the noise level as large values of the angular power spectrum for  $l = 1, 2$  and is completely consistent with what is expected. Also, note that the uncertainty in the data shown as the error bars in Figure 9, only takes into account the variation of parameters of the RTFs and a fixed  $H_0 = 70 \text{ km/s Mpc}^{-1}$ . We do not anticipate that the values of  $H_0$  (also  $q_0$ ) or so any variation in cosmology would affect distances to all the galaxies almost equivalently unless neglecting the redshift dependence in the current redshift range. Therefore, a full assessment can be warranted when  $H_0$  is utilized as a free parameter alongside the local distance calibrators, to obtain more quantitative limits on the level of isotropy. This however is not expected to change the inference here that the current galaxy sample is completely consistent with the null hypothesis of isotropy.

## 5 CONCLUSIONS AND OUTLOOK

We have presented the usefulness of the astrophysical scaling relation, in particular, the Radial Tully-Fisher Yegorova & Salucci (2007), to assess the variation in the Hubble parameter in the local universe. While similar studies have been performed using the TF relation earlier, here we use RTF for the very first time. This empirical relation exploits the information of the full RC rather than one single reference

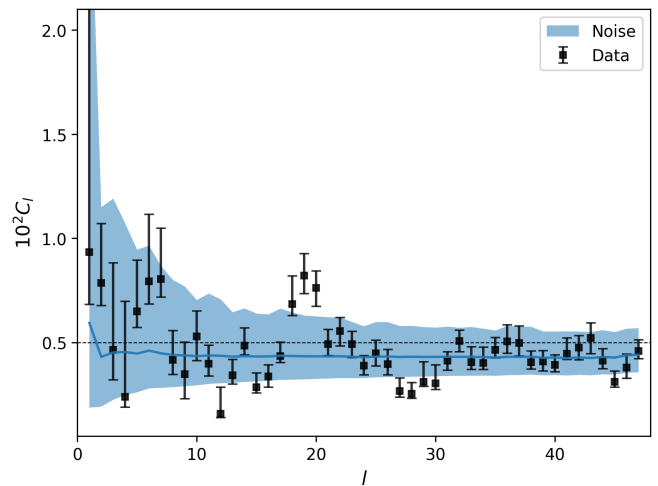


**Figure 9.** Power spectrum of the spatial clustering of the galaxies. The blue line shows the mean of the noise level, while the shaded region shows the 68% C.L. uncertainty on the noise level.

value as done using the TF relation. From a physical point of view, in contrast to the TF relation, the RTF takes into account the presence of DM in galaxies and the variation in them of the stellar mass-to-light ratios. The primary results of our analysis are summarised as follows:

- We constrain the maximum possible variance in the Hubble parameter as a function of redshift in the range of  $0.005 < z < 0.035$  to be  $\Delta H_0/H_0 \lesssim 3\%$  at 95% C.L., showing no significant redshift dependence.
- Conservatively, using only the  $0.6R_{\text{opt}}$  radial bin we find the consistent with our baseline analysis using 4 radial bins with  $\Delta H_0/H_0 \lesssim 4\%$  at 95%, estimated at  $D_L \sim 10$  [Mpc].
- These constraints allow us to conservatively conclude that any local solutions to alleviate the  $H_0$ -tension are not supported within the redshift range of the current galaxy sample.
- We introduce a joint analysis of the ‘independent’ RTF relations, reducing the number of parameters while assessing the possible correlation between them. This also provides us with a possible pseudo-standardization of the RTFs.
- While occupying only the southern hemisphere, spatial clustering of the current galaxies shows no deviation from the null hypothesis of isotropy.

Constraining the value of the present expansion rate ( $H_0$ ) is one of the most crucial aspects of the current cosmological crisis. Exploring different independent methods and possible synergies in these datasets will yield a better understanding of changing the current cosmological paradigm in a more consistent direction. Needless to say, it is important to validate the analysis with newer datasets. In this context, we intend to extend the current analysis to much larger samples of galaxies, like PROBES (Stone et al. 2022) and MANGA (Arora et al. 2021), also extending to farther redshifts (Sharma et al. 2021, 2022) to provide a comprehensive understanding of the evolution of the local and late universe. This is necessary also to validate the possible alternative inference when the innermost radial bin  $0.2 R_{\text{opt}}$  is included in the joint analysis, which in-

dicates a variation of  $\Delta H_0/H_0 \sim 10\%$ , which is sufficiently apt to explain the  $H_0$ -tension.

On the other hand, as a second installment to this pilot study, we intend to perform a joint analysis utilizing the local distance estimators (Riess et al. 2021) to calibrate the RTFs and constrain the value  $H_0$ . To this end, we have introduced here the joint analysis of the RTFs that will be a preliminary step in this direction, allowing a pseudo-standardization of the empirical Radial Tully-Fisher relations.

## ACKNOWLEDGEMENTS

The authors are grateful to Leandros Perivolaropoulos, Stephane Courteau, and Anto I. Lonappan for insightful discussions. BSH is supported by the INFN INDARK grant.

## DATA AVAILABILITY

The data products utilized in the manuscript are all publicly available and appropriately referenced. And code utilized to perform the analysis here can be made available on reasonable request soon after acceptance of the paper.

## REFERENCES

- Abdalla E., et al., 2022, *JHEAp*, 34, 49
- Addison G. E., Watts D. J., Bennett C. L., Halpern M., Hinshaw G., Weiland J. L., 2018, *Astrophys. J.*, 853, 119
- Adil S. A., Akarsu O., Di Valentino E., Nunes R. C., Özüilker E., Sen A. A., Specogna E., 2024, *Phys. Rev. D*, 109, 023527
- Aghanim N., et al., 2020, *Astron. Astrophys.*, 641, A6
- Akarsu O., Barrow J. D., Escamilla L. A., Vazquez J. A., 2020, *Phys. Rev. D*, 101, 063528
- Akarsu O., Di Valentino E., Kumar S., Nunes R. C., Vazquez J. A., Yadav A., 2023
- Akarsu O., Colgáin E. O., Sen A. A., Sheikh-Jabbari M. M., 2024
- Alam S., et al., 2021, *Physical Review D*, 103
- Alesta G., Kazantzidis L., Perivolaropoulos L., 2021, *Phys. Rev. D*, 103, 083517
- Alesta G., Camarena D., Di Valentino E., Kazantzidis L., Marra V., Nesseris S., Perivolaropoulos L., 2022, *Phys. Rev. D*, 105, 063538
- Anchordoqui L. A., 2021, *Phys. Rev. D*, 103, 035025
- Andersen R., 2009, *Annu. Rev. Sociol.*, 35, 67
- Arora N., Stone C., Courteau S., Jarrett T. H., 2021, *MNRAS*, 505, 3135
- Banerjee S., Petronikolou M., N. Saridakis E., 2023, *PoS, CORFU2022*, 263
- Benevento G., Hu W., Raveri M., 2020, *Phys. Rev. D*, 101, 103517
- Benisty D., 2023, *PoS, CORFU2022*, 259
- Bernal J. L., Verde L., Jimenez R., Kamionkowski M., Valcin D., Wandelt B. D., 2021, *Phys. Rev. D*, 103, 103533
- Bernardo R. C., Levi Said J., 2021, *JCAP*, 08, 027
- Blakeslee J. P., Jensen J. B., Ma C.-P., Milne P. A., Greene J. E., 2021, *Astrophys. J.*, 911, 65
- Blinov N., Keith C., Hooper D., 2020, *JCAP*, 06, 005
- Bonvin V., et al., 2017, *Mon. Not. Roy. Astron. Soc.*, 465, 4914
- Cai R.-G., Ding J.-F., Guo Z.-K., Wang S.-J., Yu W.-W., 2020
- Camarena D., Marra V., 2019, arXiv e-prints, p. arXiv:1910.14125
- Camarena D., Marra V., 2023
- Cao S., Ratra B., 2023, *Phys. Rev. D*, 107, 103521
- Chen G. C. F., et al., 2019, *Mon. Not. Roy. Astron. Soc.*, 490, 1743
- Cleveland W. S., 1979, *J. Am. Stat. Assoc.*
- Cleveland W. S., Devlin S. J., 1988, *J. Am. Stat. Assoc.*
- Colgáin E. Ó., Van Putten M. H. P. M., Yavartanoo H., 2018
- Cook R. D., Weisberg S., 1999, *Applied Regression Including Computing and Graphics*. John Wiley & Sons, Ltd., Chichester, England, UK, doi:10.1002/9780470316948, <https://onlinelibrary.wiley.com/doi/book/10.1002/9780470316948>
- Courteau S., 1997, *AJ*, 114, 2402
- Desmond H., Sakstein J., 2020, *Phys. Rev. D*, 102, 023007
- Desmond H., Jain B., Sakstein J., 2019, *Phys. Rev. D*, 100, 043537
- Di Valentino E., et al., 2021, *Astropart. Phys.*, 131, 102605
- Du S.-S., Wei J.-J., You Z.-Q., Chen Z.-C., Zhu Z.-H., Liang E.-W., 2023, *Mon. Not. Roy. Astron. Soc.*, 521, 4963
- Efstathiou G., 2020
- Escamilla-Rivera C., Levi Said J., Mifsud J., 2021, *JCAP*, 10, 016
- Fernández-Hernández L. M., Montiel A., Rodríguez-Meza M. A., 2019, *Mon. Not. R. Astron. Soc.*, 488, 5127
- Fontaine J.-P., et al., 2018, in 53rd Rencontres de Moriond on Cosmology. pp 363–364
- Foreman-Mackey D., Hogg D. W., Lang D., Goodman J., 2013, *PASP*, 125, 306
- Fox J., 2008, *Applied regression analysis and generalized linear models*, 2nd ed.. <https://psycnet.apa.org/record/2008-05774-000>
- Fox J., 2024, *Applied Regression Analysis and Generalized Linear Models*, <https://us.sagepub.com/en-us/nam/applied-regression-analysis-and-generalized-linear-models/book237254>
- Freedman W. L., 2021, *Astrophys. J.*, 919, 16
- Freedman W. L., et al., 2019, *Astrophys. J.*, 882, 34
- Gómez-Valent A., 2018, arXiv e-prints
- Gómez-Valent A., Favale A., Migliaccio M., Sen A. A., 2024, *Phys. Rev. D*, 109, 023525
- Haridasu B. S., Viel M., 2020, *Mon. Not. Roy. Astron. Soc.*, 497, 1757
- Haridasu B. S., Luković V. V., Moresco M., Vittorio N., 2018, *JCAP*, 1810, 015
- Haridasu B. S., Viel M., Vittorio N., 2021, *Phys. Rev. D*, 103, 063539
- Hoscheit B. L., Barger A. J., 2017, in American Astronomical Society Meeting Abstracts #230. p. 314.05
- Hu J.-P., Wang F.-Y., 2023, *Universe*, 9, 94
- Huang C. D., et al., 2019, [10.3847/1538-4357/ab5dbd](https://arxiv.org/abs/10.3847/1538-4357/ab5dbd)
- Jedamzik K., Pogosian L., Zhao G.-B., 2021, *Commun. in Phys.*, 4, 123
- Lee J., Suyu S., Komatsu E., Fassnacht C. D., Hilbert S., Koopmans L. V. E., 2019, [10.1126/science.aat7371](https://arxiv.org/abs/10.1126/science.aat7371)
- Karukes E. V., Salucci P., 2017, *MNRAS*, 465, 4703
- Karwal T., Kamionkowski M., 2016, *Phys. Rev.*, D94, 103523
- Keenan R. C., Barger A. J., Cowie L. L., 2013, *ApJ*, 775, 62
- Kenworthy W. D., Scolnic D., Riess A., 2019, *The Astrophysical Journal*, 875, 145
- Khosravi N., Baghran S., Afshordi N., Altamirano N., 2019, *Phys. Rev.*, D99, 103526
- Knox L., Millea M., 2020, *Phys. Rev. D*, 101, 043533
- Kourkchi E., Tully R. B., Anand G. S., Courtois H. M., Dupuy A., Neill J. D., Rizzi L., Seibert M., 2020, *Astrophys. J.*, 896, 3
- Kourkchi E., Tully R. B., Courtois H. M., Dupuy A., Guinet D., 2022, *MNRAS*, 511, 6160
- Kreisch C. D., Cyr-Racine F.-Y., Doré O., 2020, *Phys. Rev. D*, 101, 123505
- Krishnan C., Colgáin E. O., Sheikh-Jabbari M. M., Yang T., 2021, *Phys. Rev. D*, 103, 103509
- Lapi A., Boco L., Cueli M. M., Haridasu B. S., Ronconi T., Baccigalupi C., Danese L., 2023, *Astrophys. J.*, 959, 83
- Lee N., Ali-Haïmoud Y., Schöneberg N., Poulin V., 2023, *Phys. Rev. Lett.*, 130, 161003
- Lemos P., Lee E., Efstathiou G., Gratton S., 2019, *Mon. Not. Roy. Astron. Soc.*, 483, 4803

- Lewis A., 2019
- Li X., Liao K., 2024
- Liao K., Shafieloo A., Keeley R. E., Linder E. V., 2020, *Astrophys. J. Lett.*, 895, L29
- Liu Y., Yu H., Wu P., 2023, *Astrophys. J. Lett.*, 946, L49
- Luković V. V., Haridasu B. S., Vittorio N., 2019, *MNRAS*, p. 2671
- Lyu M.-Z., Haridasu B. S., Viel M., Xia J.-Q., 2020, *Astrophys. J.*, 900, 160
- Marra V., Perivolaropoulos L., 2021, *Phys. Rev. D*, 104, L021303
- Mathewson D. S., Ford V. L., Buchhorn M., 1992, *Astrophys. J. Suppl.*, 81, 413
- Montiel A., Lazkoz R., Sendra I., Escamilla-Rivera C., Salzano V., 2014, *Phys. Rev. D*, 89, 043007
- Mortsell E., Goobar A., Johansson J., Dhawan S., 2021
- Mortsell E., Goobar A., Johansson J., Dhawan S., 2022, *Astrophys. J.*, 935, 58
- Niedermann F., Sloth M. S., 2021a, *Phys. Rev. D*, 103, L041303
- Niedermann F., Sloth M. S., 2021b, *Phys. Rev. D*, 103, 103537
- Nygaard A., Holm E. B., Tram T., Hannestad S., 2023
- Pandey S., Raveri M., Jain B., 2020, *Phys. Rev. D*, 102, 023505
- Perivolaropoulos L., Skara F., 2022, *New Astron. Rev.*, 95, 101659
- Perivolaropoulos L., Skara F., 2023, *Mon. Not. Roy. Astron. Soc.*, 520, 5110
- Persic M., Salucci P., Stel F., 1996, *Mon. Not. Roy. Astron. Soc.*, 281, 27
- Pesce D. W., et al., 2020, *Astrophys. J. Lett.*, 891, L1
- Poulin V., 2020, in 3rd World Summit on Exploring the Dark Side of the Universe. pp 17–28
- Poulin V., Smith T. L., Bartlett A., 2021
- Qi J.-Z., Meng P., Zhang J.-F., Zhang X., 2023, *Phys. Rev. D*, 108, 063522
- Riess A. G., 2019, *Nature Rev. Phys.*, 2, 10
- Riess A. G., et al., 2016, *Astrophys. J.*, 826, 56
- Riess A. G., et al., 2018a, *Astrophys. J.*, 853, 126
- Riess A. G., et al., 2018b, *The Astrophysical Journal*, 855, 136
- Riess A. G., Casertano S., Yuan W., Bowers J. B., Macri L., Zinn J. C., Scolnic D., 2021, *Astrophys. J. Lett.*, 908, L6
- Riess A. G., et al., 2024
- Ruchika Rathore H., Roy Choudhury S., Rentala V., 2023
- Salucci P., 2008, *IAU Symp.*, 244, 53
- Salucci P., 2019, *Astron. Astrophys. Rev.*, 27, 2
- Salucci P., Burkert A., 2000, *Astrophys. J. Lett.*, 537, L9
- Salucci P., Frenk C. S., Persic M., 1993, *MNRAS*, 262, 392
- Salvatier J., Wiecki T. V., Fonnesbeck C., 2016, *PeerJ Computer Science*, 2, e55
- Schombert J., McGaugh S., Lelli F., 2020, *Astron. J.*, 160, 71
- Schöneberg N., Franco Abellán G., Pérez Sánchez A., Witte S. J., Poulin V., Lesgourgues J., 2021
- Scolnic D. M., et al., 2018, *Astrophys. J.*, 859, 101
- Seabold S., Perktold J., 2010, in 9th Python in Science Conference.
- Shah P., Lemos P., Lahav O., 2021, *Astron. Astrophys. Rev.*, 29, 9
- Shajib A. J., et al., 2020, *Mon. Not. Roy. Astron. Soc.*, 494, 6072
- Shanks T., Hogarth L. M., Metcalfe N., 2019, *MNRAS*, 484, L64
- Sharma G., Salucci P., Harrison C. M., van de Ven G., Lapi A., 2021, *MNRAS*, 503, 1753
- Sharma G., Salucci P., van de Ven G., 2022, *A&A*, 659, A40
- Solà J., Gómez-Valent A., de Cruz Pérez J., 2017, *Phys. Lett. B*, 774, 317
- Soltis J., Casertano S., Riess A. G., 2021, *Astrophys. J. Lett.*, 908, L5
- Stone C., Courteau S., Arora N., Frosst M., Jarrett T. H., 2022, *ApJS*, 262, 33
- Tristram M., et al., 2023, ] 10.1051/0004-6361/202348015
- Tully R. B., 2023
- Tutusaus I., Lamine B., Blanchard A., 2019, *A&A*, 625, A15
- Tutusaus I., Kunz M., Favre L., 2023
- Vagnozzi S., 2020, *Phys. Rev. D*, 102, 023518
- Vagnozzi S., 2023, *Universe*, 9, 393
- Vattis K., Koushiappas S. M., Loeb A., 2019, *Phys. Rev. D*, 99, 121302
- Verde L., Treu T., Riess A. G., 2019, in *Nature Astronomy* 2019. ([arXiv:1907.10625](https://arxiv.org/abs/1907.10625)), [doi:10.1038/s41550-019-0902-0](https://doi.org/10.1038/s41550-019-0902-0)
- Verde L., Schöneberg N., Gil-Marín H., 2023
- Vogt N. P., Haynes M. P., Giovanelli R., Herter T., 2004, *AJ*, 127, 3325
- Whitbourn J. R., Shanks T., 2014, *MNRAS*, 437, 2146
- Wiecki T., , in Team P., ed., , *PyMC examples*, [doi:10.5281/zenodo.5654871](https://doi.org/10.5281/zenodo.5654871).
- Wong K. C., et al., 2020, *Mon. Not. Roy. Astron. Soc.*, 498, 1420
- Yegorova I. A., Salucci P., 2007, *Mon. Not. Roy. Astron. Soc.*, 377, 507
- Yuan W., Riess A. G., Macri L. M., Casertano S., Scolnic D., 2019, *Astrophys. J.*, 886, 61
- Zhao M.-M., He D.-Z., Zhang J.-F., Zhang X., 2017, *Phys. Rev.*, D96, 043520
- Zhao G.-B., et al., 2019, *Mon. Not. Roy. Astron. Soc.*, 482, 3497
- de Jaeger T., Stahl B. E., Zheng W., Filippenko A. V., Riess A. G., Galbany L., 2020, *Mon. Not. Roy. Astron. Soc.*, 496, 3402
- de la Macorra A., Almaraz E., Garrido J., 2022, *Phys. Rev. D*, 105, 023526
- du Mas des Bourboux H., et al., 2020, *Astrophys. J.*, 901, 153

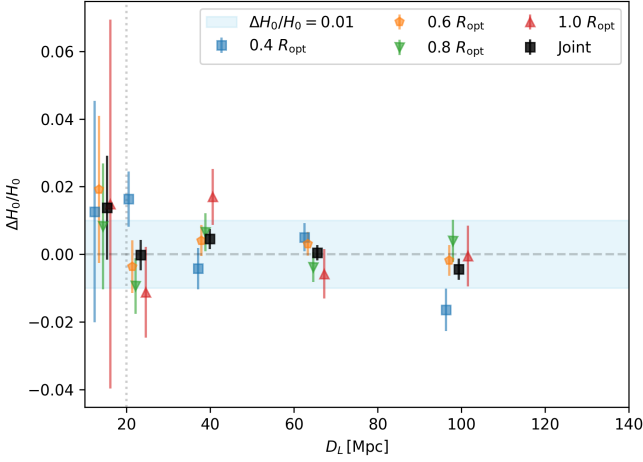


**Figure A1.** Same as Figure 5 for the logarithmic binning of distance as described in Appendix A.

## APPENDIX A: ALTERNATE BINNING OF THE DISTANCE

In the main text, we have presented our primary results using a bin size of  $\Delta D_L = 20$  [Mpc], using linear binning of the magnitude residuals. In this section, we briefly report the mild differences we notice when different binning schemes are utilized. In Figure A1 we show the  $\Delta H_0/H_0$  using a logarithmic binning scheme. We notice that the joint constraint shows a mild jump in the mean value of  $\Delta H_0/H_0$  towards lower redshifts in the closest distance bin, although with no strong significance. And while being completely consistent with  $\Delta H_0/H_0 = 0$  for distances larger than 20 [Mpc]. Note that this is particularly interesting in the context of some of the ultra late-time resolutions to  $H_0$ -tension, as we mentioned in the main text. The closest distance bins centered at  $\sim 15$  [Mpc] and  $\sim 23$  [Mpc] contain about 10, 100 galaxies in each, respectively. The most local distance bin, with very few galaxies, seems to consistently suggest a mild jump in  $H_0$ , even for our conservative  $0.6R_{\text{opt}}$  bin. This as we have already mentioned in the main text is more evident when the innermost  $0.2R_{\text{opt}}$  bin is included in the joint analysis.

## APPENDIX B: CONTOUR PLOTS OF THE JOINT ANALYSIS

For the sake of brevity in the main text, we show the contour plots of the joint analysis here. As elaborated in the main text, we can see that the slopes of the individual RTFs are correlated to a certain extent in the joint analysis, while the intrinsic scatters of the same have negligible correlation. Also, one can notice that the intrinsic scatter of the bin  $\sigma_n(0.6R_{\text{opt}})$  almost shows lower intrinsic scatter, validating that this radial bin is well constrained. Similarly, also the slope  $a_n(0.6R_{\text{opt}})$  can be seen to have negligible correlation with the rest of the RTFs slopes.

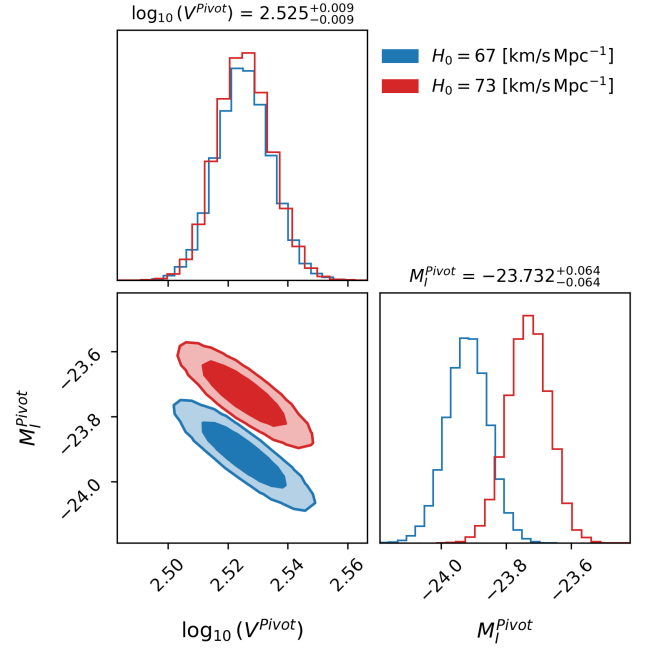


**Figure B1.** We show the 68% and 95% C.L. posteriors for the parameters  $\log_{10}(V^{\text{Pivot}})$  and  $M_I^{\text{Pivot}}$ , when the likelihood analysis is performed assuming  $H_0 = 67$  km/s Mpc $^{-1}$  (blue) and  $H_0 = 73$  km/s Mpc $^{-1}$  (red). The  $1\sigma$  parameter constraints for the case of  $H_0 = 73$  km/s Mpc $^{-1}$  are shown on top of the 1D posteriors.

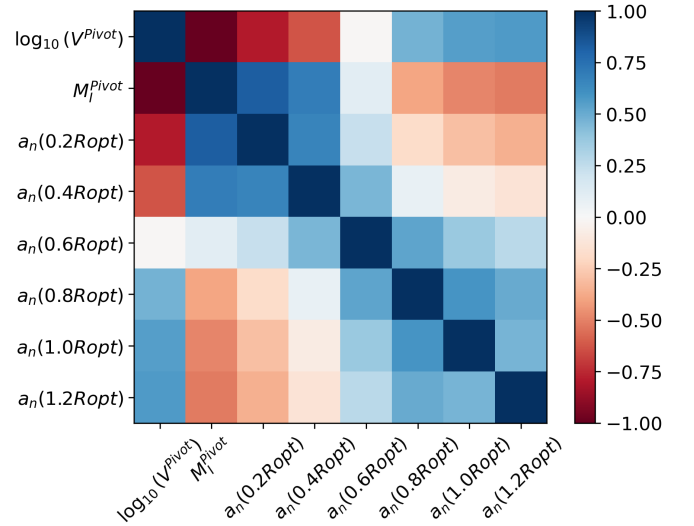


**Figure B2.** Correlation between the posteriors of the estimated slopes for the individual RTF relations and the pivot point.

This paper has been typeset from a  $\text{\TeX}/\text{\LaTeX}$  file prepared by the author.

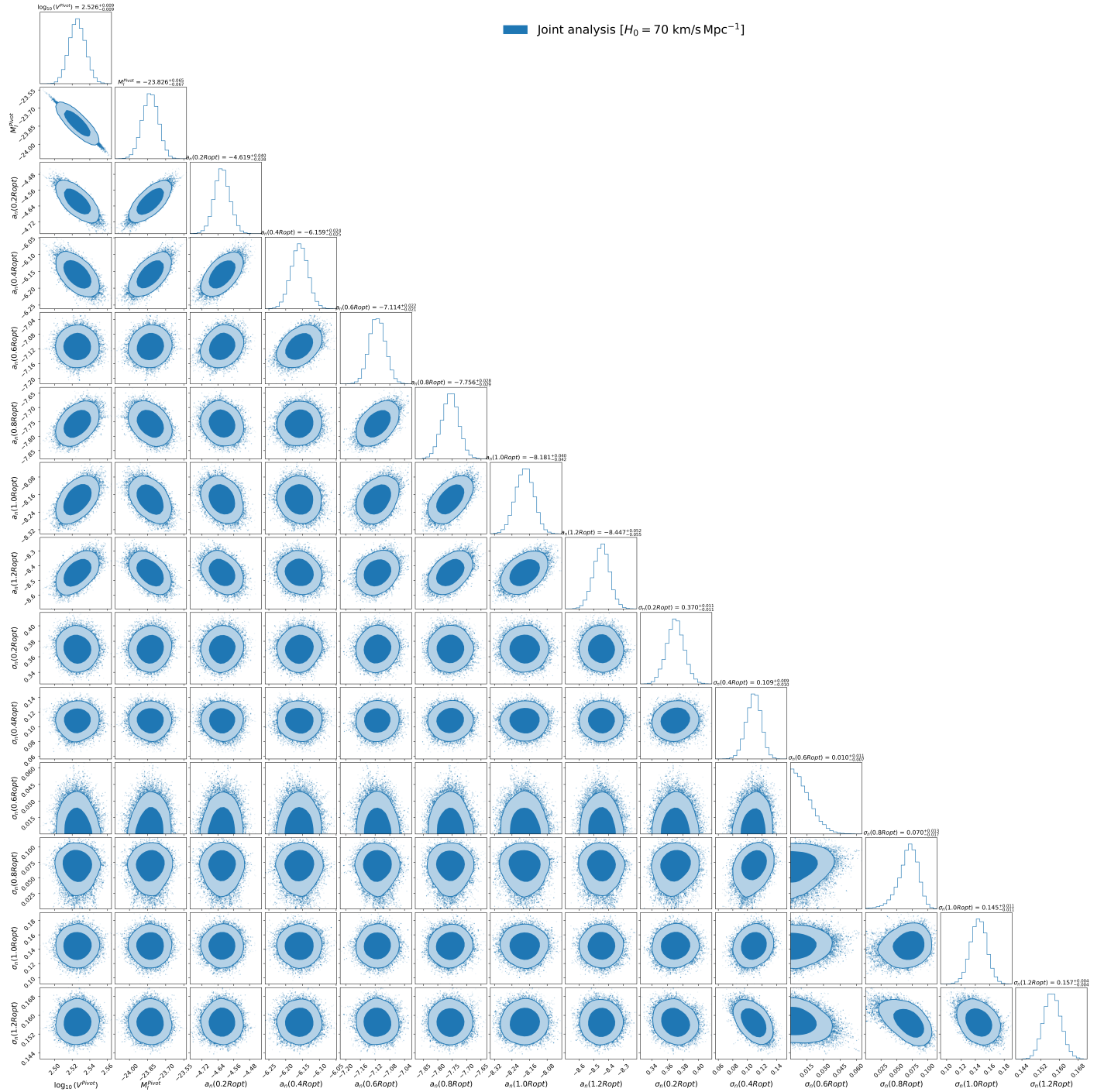


**Figure B3.** Contour plots showing the 68% and 95% C.L. for all the parameters in the joint analysis of the RTFs. We assume the  $H_0 = 70 \text{ km/s Mpc}^{-1}$ .